Sound & Vibration 2026, 60(6), 4679.
doi: https://doi.org/10.59400/sv4679

Article

Interval type-2 fuzzy fractional harmonic-balance optimization of a quasi-zero-stiffness isolator for robust low-frequency vibration suppression

Suleiman Ibrahim Mohammad[1], Yogeesh Nijalingappa[1,2,3,*], Seif Al Bustanji[4,5], Poornachandran William[6,7], Asokan Vasudevan[8], Torki M. Al-Fawwaz[9]

[1] Research Fellow, INTI International University, Nilai 71800, Malaysia; dr_sliman@yahoo.com
[2] Mathematics & Natural Sciences, Gulf University for Science & Technology, Safat 13060, Kuwait
[3] Department of Mathematics, Government First Grade College, Tumkur 572102, India
[4] Faculty of Technical Education, Al-Ahliyya Amman University, Amman 19328, Jordan; s.albustanji@ammanu.edu.jo
[5] Hourani Center for Applied Scientific Research (HCASR), Al-Ahliyya Amman University, Amman 19328, Jordan
[6] School of Computer Science and Technology, Karunya Institute of Technology and Sciences, Coimbatore 641114, India; williamp@karunya.edu
[7] Centre for Research and Consultancy, UNITAR International University, Petaling Jaya 47301, Malaysia
[8] Faculty of Business and Communications, INTI International University, Nilai 71800, Malaysia; asokan.vasudevan@newinti.edu.my
[9] College of Commerce and Business, Lusail University, Lusail P.O. Box 9717, Qatar; talfawwaz@lu.edu.qa
*** Corresponding author:** Yogeesh Nijalingappa, yogeesh.n@ka.gov.in

CITATION

Mohammad SI, Nijalingappa Y, Al Bustanji S, et al. Interval type-2 fuzzy fractional harmonic-balance optimization of a quasi-zero-stiffness isolator for robust low-frequency vibration suppression. Sound & Vibration. 2026; 60(6): 4679. https://doi.org/10.59400/sv4679

ARTICLE INFO

Received: 20 July 2026
Revised: 15 August 2026
Accepted: 21 August 2026
Available online: 1 September 2026

Abstract: Quasi-zero-stiffness (QZS) isolators possess a combination of high load capacity and low dynamic stiffness; however, their characteristics are sensitive to geometric nonlinearity, frequency-dependent dissipation, excitation amplitude and epistemic uncertainty. In this study, a new design scheme is proposed to produce the constant geometric restoring force of a three-spring QZS isolator subject to base excitation. Caputo fractional damping + exact first-harmonic stiffness (in terms of complete elliptic integrals) + multi-harmonic alternating frequency–time harmonic balance (to check the harmonic content and residual error). Interval type-2 fuzzy numbers account for uncertainty in the following quantities: geometric ratio, residual tangent stiffness, fractional damping intensity (or order), and base-motion amplitude. Differential evolution of upper-tail resonance risk and lower-tail isolation losses. A limiting-case validation against a literature benchmark verifies that the fractional-order models recover the classic viscously damped three-spring QZS equations for the case of approaching finite response amplitude and unity fractional order. For the 50 kg realization, the optimized design has a geometric ratio of 1.1824, residual stiffness of 0.02110, damping ratio of 0.02581 and fractional order of 0.9063. Its 95th-percentile peak transmissibility is 3.358 across 120 outer-footprint scenarios, which is 28.9% below the optimized viscous-limit QZS reference. Adverse-tail isolation onset is 23.3% earlier than deterministic fractional tuning completion, and adverse-tail mean attenuation improvements are as high as 1.08 dB. The five-harmonic verification ensures that the ratio of the third harmonic stays below 0.31% in all ranges mentioned in operating range.

Keywords: quasi-zero stiffness; fractional calculus; interval type-2 fuzzy set; harmonic balance; robust optimization; nonlinear vibration isolation; epistemic uncertainty

1. Introduction

Passive linear supports should sustain static weights, while maintaining a dynamically compliant behaviour, making low-frequency vibration isolation challenging. The introduction of the stability stiffens when the natural frequency increases but is large load-bearing capacity and vice versa reduces the isolation capillary force. This contradiction is overcome by high-static–low-dynamic-stiffness and quasi-zero-stiffness mechanisms, which achieve a combined negative-stiffness correction of the positive-stiffness load path close to the operating equilibrium. This yields small tangent stiffness while the global potential is bounded and the statically supported mass remains in a state of stable equilibrium [1–4]. Such mechanisms provide a geometry-based route for improving vibration protection at low frequencies in vibration-sensitive systems [2–4].

The force law of the classical three-spring configuration follows directly from geometry; therefore, it can be derived without empirical curve fitting. The payload is suspended by a vertical spring, and the two other symmetric inclined springs bring in an additional displacement-dependent negative stiffness. Dynamic analyses have identified geometric conditions leading to zero or near-zero tangent stiffness [2,3]. As shown in dynamic analyses, the very same nonlinearity can lead to a softening response, amplitude-dependent resonance, jump phenomena and an influence on performance due to preload and manufacturing error [3, 4]. More advanced QZS designs use magnetic springs, buckled beams, cam–roller arrangements [5–9], torsional solutions, origami or even electromagnetic tuning [10–14]. Because the simple three-spring system has an exact restoring force that can be expressed without phenomenological fitting, it is still an important mathematical benchmark despite these advances.

The classical viscous damping assumption is integer-order in most QZS studies. This approximation is useful but can be misleading when dissipation originates from polymers, elastomeric joints, laminated interfaces, viscoelastic pads or hereditary friction [15–17]. The fractional derivatives have been shown to be a compact phenomenological representation of both power-law memory and frequency-dependent phase lag [18–20]. The single fractional order helps to maintain parsimonious parameterization, which can interpolate between spring-like (2-norm) and dashpot-like (1-norm). The fractional operator in this formula adds a term that is in-phase with the input and an out-of-phase term that depends on some fractional frequency power. This feature couples to the effective dynamic stiffness of the structure, which also depends on QZS geometry and thus contributes nontrivially to the resonance peak.

The second challenge lies in the nonlinear solution itself. As important examples, cubic Taylor expansions and single-term harmonic balance have gained popularity because they produce amplitude equations that are straightforward to interpret. Modelling with a cubic polynomial is not accurate for slanted springs under large deflections, and one harmonic approximation conceals higher harmonics or multiple branches. The alternating frequency-time (AFT) method calculates the nonlinear restoring force on a time grid and passes it to Fourier coefficients without explicit polynomial expansion [21, 22]. The associated harmonic/Galerkin formulation is consistent with established nonlinear-oscillation methods [23,24]. It therefore allows the exact geometric principle to be incorporated together with multi-harmonic balance. An exact elliptic-integral fundamental stiffness is used for an efficient global search, and an AFT multi-harmonic solution provides independent verification.

A third difficulty is uncertainty. The small tangent stiffness resulting from the negative-stiffness cancellation also magnifies sensitivities to geometric tolerance, stiffness drift, damping variability, excitation level and installation error. Thus, a purely deterministic optimum may be sharply tuned but fragile. Reliable probability distributions are difficult to obtain in an early design stage where no prototype exists and only tolerances/expert intervals or rare observations can be used. Type-1 fuzzy numbers encode values over an interval with graded plausibility [25]. Interval type-2 (IT2) fuzzy sets introduce a footprint of uncertainty identified by upper and lower membership functions, thereby retaining uncertainty about the membership grade itself [26–30]. This additional layer is useful when experts, models, batches, or operational conditions provide inconsistent tolerance descriptions.

The principal research question is therefore: which combinations of geometry and fractional damping maintain low-frequency isolation when the exact passive QZS equations are propagated through an IT2 fuzzy parameter footprint? Recent QZS studies have advanced compliant and magnetic mechanisms [5–9], along with metamaterial and experimentally verified mechanisms [10–14], while adjacent structural-vibration studies have combined fractional dynamics with type-2 fuzzy control [29–32]. However, those control-oriented studies use fuzzy inference or active control rather than propagating an IT2 parameter footprint through exact passive QZS mechanics; conversely, the cited QZS studies do not combine exact finite-rotation mechanics, Caputo damping, IT2 alpha-plane co-design, and multi-harmonic verification in one framework. The gap claimed here is therefore this specific integration, not fuzzy nonlinear vibration analysis in general.

Details of the contributions are as follows. First, we derive exact dimensionless geometric force, tangent stiffness, potential energy and local stability conditions. Second, a Caputo-like fractional damping model is adopted and split into storage- and loss-type frequency components. Third, we obtain a precise first-harmonic nonlinear stiffness in terms of complete elliptic integrals, thus bypassing the cubic truncation implemented during optimization. Fourth, a multi-harmonic AFT formulation checks for residual norms and harmonic convergence. Fifth, an IT2 fuzzy alpha–plane model of five uncertain quantities is defined and its outer support is sampled (without probability density constraints). Finally, an optimization of a lower-tail/upper-tail robust objective is implemented and compared with a linear reference, viscous-limit QZS design, and deterministically tuned fractional QZS designs. All numerical setups and outcomes required to check the presented results are incorporated into the paper.

The integrated physical and computational architecture is shown in **Figure 1**. The left-side panel specifies the precise QZS mechanism and relative coordinate. The right-side panel shows the sequence from geometric mechanics, fractional dynamics, to AFT verification, IT2 uncertainty propagation, robust search, and convergence assessment.

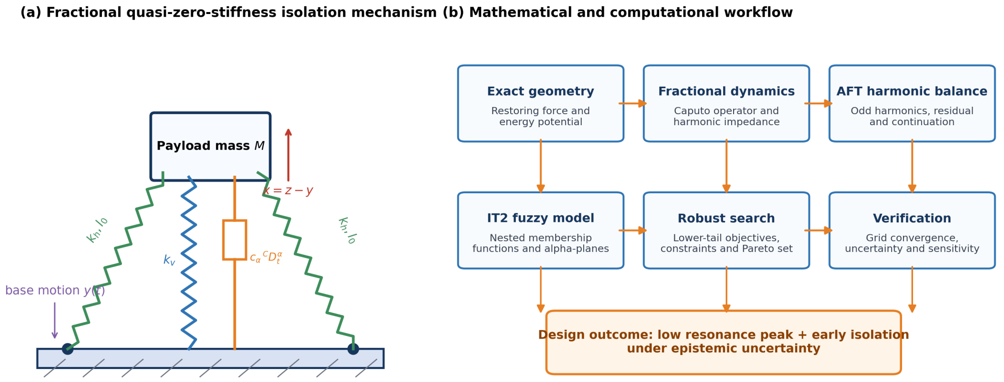

Figure 1. Exact three-spring fractional QZS isolator and the mathematical–computational workflow used for robust design and verification.

2. Exact nonlinear fractional model

2.1. Geometry, coordinates, and force equilibrium

Consider a payload of mass M undergoing vertical motion with absolute displacement $z(t)$. The base undergoes harmonic motion $y(t) = Y\cos(\Omega t)$ and the relative displacement $x(t) = z(t) - y(t)$. In the considered configuration, a vertical spring (k_v) acting in parallel with two identical inclined springs (k_h), at the reference equilibrium, the horizontal half-span is denoted a and the free-length of each inclined spring l_0. The instantaneous inclined-spring length is

$$l(x) = \sqrt{a^2 + x^2}. \tag{1}$$

The axial force in each inclined spring equals $k_h\,[l(x) - l_0]$ and its vertical component is $k_h\,[l(x) - l_0]\,x/l(x)$. Adding the vertical spring gives the exact restoring force measured from equilibrium,

$$F_s(x) = k_v x + 2k_h x\left(1 - \frac{l_0}{\sqrt{a^2 + x^2}}\right). \tag{2}$$

No polynomial approximation is used in this force law and the dimensional equation under base acceleration is

$$M\ddot{x} + c_\alpha\,\mathcal{D}_t^\alpha x + F_s(x) = -M\ddot{y}. \tag{3}$$

where $0 < \alpha \le 1$, c_α has units $N\,\frac{s^\alpha}{m}$, and $\mathcal{D}_t^\alpha$ denotes the Caputo derivative. For zero initial-history terms, its definition is

$$\mathcal{D}_t^\alpha x(t) = \frac{1}{\Gamma(1-\alpha)}\int_0^t \frac{\dot{x}(\xi)}{(t-\xi)^\alpha}\,d\xi. \tag{4}$$

The Caputo form allows traditional displacement and velocity initial conditions, resulting in a memory kernel that is physically interpretable. For $\alpha = 1$, the damping term simplifies to a normal viscous force. For $0 < \alpha < 1$, the force has a memory of past velocity distributed over time.

2.2. Dimensionless formulation

The dimensionless variables and ratios used in this study are

$$u = \frac{x}{a}, \qquad \tau = \omega_0 t, \qquad r = \frac{\Omega}{\omega_0}, \qquad \omega_0 = \sqrt{\frac{2k_h}{M}}, \tag{5}$$

$$\lambda = \frac{l_0}{a}, \qquad \kappa = \frac{k_v}{2k_h}, \qquad \delta = \kappa + 1 - \lambda, \qquad \bar{Y} = \frac{Y}{a}. \tag{6}$$

The parameter δ is the residual tangent stiffness in equilibrium. In the case of a stable QZS design, it is small and positive. The dimensionless fractional damping ratio is given by

$$2\zeta = \frac{c_\alpha \omega_0^\alpha}{2k_h}. \tag{7}$$

After division by $2k_h a$, the governing equation becomes

$$u'' + 2\zeta\, \mathcal{D}_\tau^\alpha u + g(u) = \bar{Y} r^2 \cos(r\tau), \tag{8}$$

Here, where a prime denotes differentiation with respect to τ and

$$g(u) = u\left(\lambda + \delta - \frac{\lambda}{\sqrt{1+u^2}}\right). \tag{9}$$

The exact tangent stiffness is

$$k_t(u) = \frac{dg}{du} = \lambda + \delta - \frac{\lambda}{(1+u^2)^{3/2}}. \tag{10}$$

Integration of $g(u)$ gives the dimensionless potential energy,

$$\mathit{\Pi}(u) = \frac{1}{2}(\lambda + \delta)u^2 - \lambda\left(\sqrt{1+u^2} - 1\right). \tag{11}$$

At equilibrium, $g(0) = 0$, $k_t(0) = \delta$, and $\mathit{\Pi}''(0) = \delta$. Therefore, local stability requires

$$\delta > 0. \tag{12}$$

The corresponding vertical spring ratio is $\kappa = \lambda - 1 + \delta$. Physical realizability further requires $\kappa > 0$, or $\lambda + \delta > 1$. The first non-zero terms of the exact restoring force are obtained below by expanding $\left(1 + u^2\right)^{-1/2}$,

$$g(u) = \delta u + \frac{\lambda}{2}u^3 - \frac{3\lambda}{8}u^5 + \frac{5\lambda}{16}u^7 + \cdots. \tag{13}$$

In summary, this expansion reveals that the near-equilibrium response is hardening for positive λ but with alternating higher-order contributions, further demonstrating that a cubic-only model cannot be expected to remain valid at larger amplitude. The exact formulation preserves the same square-root law while retaining higher-order accuracy.

Table 1 reports the nominal dimensional parameters and derived frequency scale used for the laboratory-scale payload support; these values do not affect the dimensionless conclusions.

Table 1. Dimensional realization and baseline analysis settings.

Quantity	Symbol	Value	Unit or interpretation
Supported mass	M	50.0	kg
Inclined-spring stiffness	k_h	25,000	N/m per spring
Horizontal half-span	a	0.080	m
Reference circular frequency	ω_0	31.6228	rad/s
Reference frequency	f_0	5.0329	Hz
Nominal base-amplitude ratio	$\bar{Y}$	0.025	dimensionless
Frequency-ratio domain	r	0.12–3.20	dimensionless
Nominal response grid	N_r	160	frequency points
AFT time samples	N_t	512–1,024	equispaced samples
Retained harmonics	$\mathcal{H}$	{1,3,5}	odd harmonics

2.3. Frequency-domain representation of fractional damping

In the present formulation, for a periodic harmonic $e^{inr\tau}$, the steady-state fractional operator satisfies

$$\mathcal{D}_\tau^\alpha e^{inr\tau} = (inr)^\alpha e^{inr\tau}. \tag{14}$$

Using the principal branch,

$$(inr)^\alpha = (nr)^\alpha e^{i\pi\alpha/2}. \tag{15}$$

The real and imaginary components then follow directly. The real part is a frequency-dependent stiffness correction and the imaginary part provides dissipation. Define

$$K_{\alpha,n} = 2\zeta(nr)^\alpha \cos(\pi\alpha/2), \tag{16}$$

$$C_{\alpha,n} = 2\zeta(nr)^\alpha \sin(\pi\alpha/2). \tag{17}$$

For $\alpha = 1$, $K_{\alpha,n} = 0$ and $C_{\alpha,n} = 2\zeta nr$, recovering viscous damping. For α < 1, both terms do not vanish. Hence, varying α is not (only) changing the damping magnitude; it also changes the dynamic stiffness.

3. Harmonic-balance solution and stability measures

3.1. Exact fundamental stiffness through elliptic integrals

For efficient design search, assume a dominant fundamental relative motion

$$u(\tau) = A\cos(r\tau - \phi). \tag{18}$$

The first cosine coefficient of $g(u)$ defines an amplitude-dependent effective stiffness,

$$k_{\text{eff}}(A) = \frac{1}{\pi A}\int_0^{2\pi} g\left(A\cos\theta\right)\cos\theta\, d\theta. \tag{19}$$

Substitution of the exact force law gives

$$k_{\text{eff}}(A) = \lambda + \delta - \lambda J(A), \tag{20}$$

$$J(A)=\frac{1}{\pi}\int_0^{2\pi}\frac{\cos^2\theta}{\sqrt{1+A^2\cos^2\theta}}\,d\theta. \tag{21}$$

Let $K(m)$ and $E(m)$ be complete elliptic integrals of the first and second kinds with parameter m. The integral is evaluated exactly as

$$J(A)=\frac{4}{\pi A^2}\left[E\left(-A^2\right)-K\left(-A^2\right)\right]. \tag{22}$$

The removable singularity at $A=0$ is handled by the series

$$J(A)=1-\frac{3}{8}A^2+\frac{15}{64}A^4-\frac{175}{1,024}A^6+O\left(A^8\right). \tag{23}$$

Consequently, the exact fundamental dynamic-stiffness components are

$$D_R(A,r)=k_{eff}(A)-r^2+2\zeta r^{\alpha}\cos\left(\frac{\pi\alpha}{2}\right), \tag{24}$$

$$D_I(r)=2\zeta r^{\alpha}\sin\left(\frac{\pi\alpha}{2}\right). \tag{25}$$

Equating the squared forcing and response amplitudes yields the nonlinear scalar amplitude equation

$$A^2\left[D_R^2(A,r)+D_I^2(r)\right]=\bar{Y}^2r^4. \tag{26}$$

The phase and complex fundamental coefficient are

$$\phi=\tan^{-1}\left(\frac{D_I}{D_R}\right),\qquad U_1=Ae^{-i\phi}. \tag{27}$$

The amplitude equation is solved by bracketed root finding on a mixed logarithmic–linear amplitude grid. When several positive roots exist, upward and downward frequency continuation select the nearest root to the preceding solution. This strategy allows branch multiplicity to be detected instead of being hidden by a fixed-point iteration.

3.2. Multi-harmonic AFT formulation

The independent verification model retains odd harmonics,

$$u(\tau)=\Re\left\{\sum_{n=1,3,5}U_ne^{inr\tau}\right\}. \tag{28}$$

At N_t equally spaced phase points $\theta_j=2\pi j/N_t$, the trial displacement is transformed to the time domain, the exact nonlinear force $g\left[u\left(\theta_j\right)\right]$ is evaluated pointwise, and a discrete Fourier transform gives its coefficients G_n. The residual for each retained harmonic is

$$R_n=Z_nU_n+G_n-F_n, \tag{29}$$

$$Z_n=-(nr)^2+2\zeta(inr)^{\alpha}, \tag{30}$$

where

$$F_n = \begin{cases} \bar{Y}r^2, & n = 1, \\ 0, & n = 3, 5. \end{cases} \tag{31}$$

The nonlinear algebraic system consists of the real and imaginary parts of $R_n = 0$. A Newton-type root solver is initialized from the preceding frequency point. The normalized residual is

$$\varepsilon_R = \left(\sum_{n \in \mathcal{H}} |R_n|^2 \right)^{1/2}. \tag{32}$$

The absolute displacement of the payload equals $z = y + x$. Using orthogonality of the harmonics, the root-mean-square displacement transmissibility is

$$T = \frac{\left(\left| \bar{Y} + U_1 \right|^2 + \sum_{n \in \mathcal{H},\, n>1} |U_n|^2 \right)^{1/2}}{\bar{Y}}. \tag{33}$$

For the fundamental model, the sum over higher harmonics vanishes. The logarithmic spectral level is $L_T = 20 \log_{10} T$. Isolation occurs when $T \leq 1$ or $L_T \leq 0$ dB.

3.3. Stability indicator for fundamental roots

A complete Floquet analysis of a fractional nonlinear system is computationally expensive inside a robust optimization loop. A local frequency-response indicator is therefore used to classify fold proximity. Define the amplitude residual

$$\mathcal{F}(A, r) = A^2 \left[D_R^2(A, r) + D_I^2(r) \right] - \bar{Y}^2 r^4. \tag{34}$$

A simple root satisfies $\partial \mathcal{F} / \partial A \neq 0$, while a saddle-node turning point satisfies

$$\mathcal{F}(A, r) = 0, \qquad \frac{\partial \mathcal{F}}{\partial A} = 0. \tag{35}$$

The derivative is analytical except we use a centered complex-safe difference for the elliptic-integral derivative. Then, the upward and downward continuations are compared. The slight overlap of branches and nonzero slope reveals a single free steady-state solution within the range tested. This is not a true fractional Floquet calculation and should only be understood as a branch-screening test for this design. The indicator tests only the simplicity (or otherwise) of algebraic roots and whether continuations are consistent; it does neither stability in orbit nor basin of attraction measurements.

4. Interval type-2 fuzzy uncertainty model

4.1. Trapezoidal footprints of uncertainty

Five quantities are uncertain: λ, δ, ζ, α, and $\bar{Y}$. Each is represented by an interval type-2 fuzzy number $\widetilde{p}$ with lower and upper trapezoidal membership functions. For a trapezoid with breakpoints (a, b, c, d), the membership function is

$$\mu(p)=\begin{cases}0, & p\le a,\\ (p-a)/(b-a), & a<p<b,\\ 1, & b\le p\le c,\\ (d-p)/(d-c), & c<p<d,\\ 0, & p\ge d.\end{cases} \tag{36}$$

The upper membership function (UMF) and lower membership function (LMF) satisfy

$$0\le \underline{\mu}_{\widetilde{p}}(p)\le \overline{\mu}_{\widetilde{p}}(p)\le 1. \tag{37}$$

Their footprint of uncertainty is

$$\mathrm{FOU}\left(\widetilde{p}\right)=\bigcup_{p}\left[\underline{\mu}_{\widetilde{p}}(p),\overline{\mu}_{\widetilde{p}}(p)\right]. \tag{38}$$

The outer UMF support reflects the widest credible tolerance, whereas the LMF identifies the more consistently supported region. The numerical percentages are listed in **Table 2**. A relative percentage is applied multiplicatively, except for α, for which the stated values are absolute half-widths.

Table 2. Design bounds and interval type-2 fuzzy half-widths about each nominal value.

Parameter	Search bound	UMF support	UMF core	LMF support	LMF core
Geometric ratio λ	1.08–1.65	±2.5%	±0.8%	±1.7%	±0.4%
Residual stiffness δ	0.015–0.140	±22%	±8%	±15%	±4%
Fractional damping ζ	0.012–0.120	±18%	±6%	±12%	±3%
Fractional order α	0.42–0.98	±0.035	±0.012	±0.024	±0.006
Base ratio $\bar{Y}$	Fixed nominal 0.025	±20%	±8%	±13%	±4%

4.2. Alpha-plane propagation

At membership level $\eta\in[0,1]$, the nested interval for parameter p is denoted $[p_L(\eta),p_U(\eta)]$. To expose the contraction from the outer footprint to the core, the numerical alpha-plane half-width is written

$$h_p(\eta)=h_p^{\mathrm{out}}(1-0.65\eta). \tag{39}$$

A standardized sample $s_p\in[-1,1]$ produces

$$p\left(\eta,s_p\right)=p_0\left[1+h_p(\eta)s_p\right] \tag{40}$$

for relative parameters, while

$$\alpha\left(\eta,s_\alpha\right)=\alpha_0+h_\alpha(\eta)s_\alpha \tag{41}$$

is used for the derivative order. This contraction is a numerical representation of the nested IT2 footprint; it does not assign probability to membership grades. Latin hypercube sampling provides space-filling points in each alpha-plane [31]. The same standardized samples are used for competing designs to reduce comparison noise. The coefficient in Equation (39) is not a fitted response parameter. Linear interpolation between an outer support half-width h_p^{out} and a core half-width h_p^{core} gives $h_p(\eta) = h_p^{out} - \eta(h_p^{out} - h_p^{core}) = h_p^{out}(1 - \kappa_{p\eta})$, where $\kappa_p = 1 - \frac{h_p^{core}}{h_p^{out}}$. For the five UMF ratios in **Table 2**, the mean contraction is $1 - \frac{\left[\left(\frac{0.8}{2.5}\right)+\left(\frac{8}{22}\right)+\left(\frac{6}{18}\right)+\left(\frac{0.012}{0.035}\right)+\left(\frac{8}{20}\right)\right]}{5} = 0.648$, which is rounded to 0.65 in Equation (39) to apply a common normalized contraction across dimensions. Thus, 0.65 is specific to the stated footprints and must be recomputed if their support or core widths change.

For any scalar performance measure $q(p)$, the fuzzy response at level η is summarized by its 5th, 50th, and 95th sample percentiles,

$$Q_q(\eta) = \left[q_{0.05}(\eta), q_{0.50}(\eta), q_{0.95}(\eta)\right]. \tag{42}$$

These are sampling summaries of a possibility domain, not frequentist confidence intervals. They are used because exact vertex propagation would require 2^5 combinations at every alpha-plane and frequency, while nonlinearity makes interior extrema possible.

5. Robust optimization problem

5.1. Performance measures

Five response measures are evaluated. The resonance measure is the maximum transmissibility over $0.15 \le r \le 1.8$,

$$J_1 = \max_{0.15 \le r \le 1.8} T(r). \tag{43}$$

The sustained isolation onset is the first frequency ratio after the global response peak for which all subsequent calculated points satisfy $T \le 1$,

$$J_2 = \min\{r_j > r_{\text{peak}} : T(r_k) \le 1 \ \forall k \ge j\}. \tag{44}$$

The mean isolation level and its 95th spectral percentile over $1.2 \le r \le 3.0$ are

$$J_3 = \frac{1}{N_I} \sum_{r_j \in I} 20 \log_{10} T(r_j), \tag{45}$$

$$J_4 = q_{0.95}\{20 \log_{10} T(r_j) : r_j \in I\}. \tag{46}$$

The largest relative motion, normalized by base amplitude, is

$$J_5 = \max_r \frac{A(r)}{\bar{Y}}. \tag{47}$$

Low values of J_1, J_2, J_4, and J_5 are desirable; more negative J_3 is desirable. The robust scalar objective combines outer-scenario 95th percentiles and a damping regularization,

$$\mathcal{J} = 0.34\widehat{J}_1 + 0.27\widehat{J}_2 + 0.22\widehat{J}_3 + 0.07\widehat{J}_4 + 0.10\widehat{\zeta} + P. \tag{48}$$

The normalized quantities in the objective are

$$\widehat{J}_1 = \frac{q_{0.95}\left(J_1\right)}{5}, \quad \widehat{J}_2 = \frac{q_{0.95}\left(J_2\right)}{2}, \quad \widehat{\zeta} = \frac{\zeta}{0.12}, \tag{49}$$

$$\widehat{J}_3 = \frac{q_{0.95}\left(J_3\right) + 20}{20}, \quad \widehat{J}_4 = \frac{q_{0.95}\left(J_4\right) + 15}{20}. \tag{50}$$

The penalty P discourages an excessive relative-motion ratio and a residual stiffness below the stability margin,

$$P = P_A + P_\delta, \tag{51}$$

$$P_A = 0.35 \max\left[0, \frac{q_{0.95}\left(J_5\right) - 18}{18}\right], \tag{52}$$

$$P_\delta = 0.20 \max\left[0, \frac{0.022 - \delta}{0.022}\right]. \tag{53}$$

The weights were fixed a priori to represent the following priority order: robust peak control > isolation time > broadband attenuation > high percentile spectral control > damping effort. The design is accomplished only if all bounds in **Table 2** and the geometric conditions $\delta > 0$ and $\lambda + \delta > 1$ are fulfilled. The numeric weights were chosen a priori by the authors as design considerations rather than being tuned to any particular engineering specification of an application; they were not validated independently. Varying these shifts the chosen solution across the reported Pareto trade-off, such that applications focused on resonance reduction, isolation initiation, or broadband attenuation should reselect weights and re-optimize. This sensitivity is qualitatively supported by the Pareto sample but not formally quantified in a weight-sweep study.

5.2. Search and verification protocol

The amplitude equation is nonconvex (which means it can change branch), and so differential evolution is used here [33, 34]. The strong search features a population of 40, 29 generations (including generation zero), ten outer-footprint scenarios per candidate, and an ultimate local polishing move. A 90-point frequency grid is used in the search. The best scenario is then evaluated on 160 points and validated with respect to independent outer-footprint Latin hypercube scenarios (n = 120) [35]. The fuzzy rule set Alpha-plane contraction uses 50 independent points for five membership levels. We keep 350 design-space samples for Pareto visualization. Spearman rank correlation is used for monotonic global sensitivity because the metric–parameter relationships are nonlinear and not necessarily affine [36,37]. The search stopped after the fixed 29-generation budget and final local polishing; no proof of global optimality is claimed. Repeated independent initial populations and cross-algorithm comparisons were not performed in the present study, so the reported design is the best solution found under the stated budget; multi-start and alternative-algorithm checks remain necessary before optimizer-level certification. Related studies also report optimized active-control placement in smart civil structures [38], UAV-enabled structural-health monitoring [39], and experimentally verified pulley-amplified multistory vibration control [40], providing broader context for optimization, monitoring, and physical validation.

The robust design is compared with three references: (i) a linear isolator with unit dimensionless stiffness and damping ratio 0.04; (ii) an independently tuned viscous-limit QZS design with $\alpha = 0.98$; and (iii) an independently tuned deterministic fractional QZS design based only on nominal response. The optimized variables and their physical mapping are given in **Table 3**.

Table 3. Optimized dimensionless designs and physical realization of the proposed robust design.

Design	λ	δ	ζ	α	κ	k_v (N/m)	l_0 (m)	c_α (N·s^α·m^{-1})
Viscous-limit QZS	1.11827	0.02095	0.02013	0.9800	0.13921	—	—	—
Deterministic fractional QZS	1.55240	0.02606	0.03209	0.6146	0.57846	—	—	—
IT2-robust fractional QZS	1.18239	0.02110	0.02581	0.9063	0.20349	10,174.53	0.094591	112.78

6. Results

6.1. Exact nonlinear mechanics

The static mechanics of the proposed design are examined in **Figure 2**. The restoring force passes through the origin only once and the tangent stiffness is positive for the portion of the operating domain displayed. At the origin, the slope is a residual small term ($\delta = 0.02110$); therefore, stiffness increases with distance as inclined springs rotate upwards. The potential energy has one stable minimum at the equilibrium. These observations validate that the nominal geometry can achieve low dynamic stiffness without establishing a local bistable well.

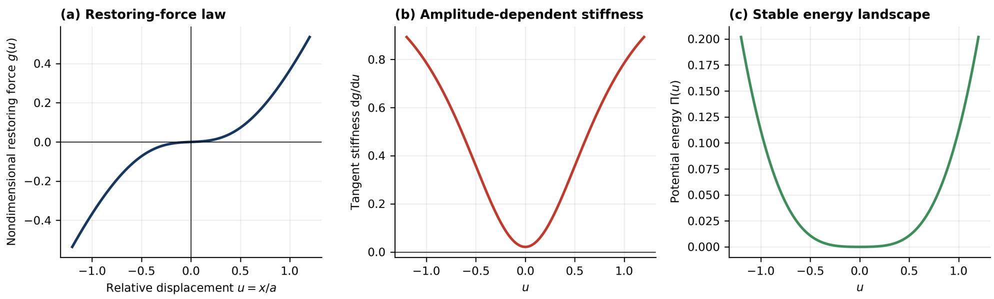

Figure 2. Exact restoring force, tangent stiffness and potential energy from the proposed QZS design; comparison with the cubic approximation indicates its validity only over a small amplitude range.

That comparison demonstrates that the cubic fit increasingly overpredicts linearity in the restoring force as amplitude increases. Near-amplitude-1, contributions at 5th and even 7th order are not negligible. Keeping the square-root law allows avoiding a spurious decrease of model resilience under high base amplitude uncertain situations.

Literature-benchmark limiting cases

The implementation was checked against the classical three-spring QZS benchmark of Carrella et al. [2] and Kovacic et al. [3]. Setting the fractional order to one recovers the conventional viscous term; taking the response-amplitude limit $A \to 0$ makes the elliptic-integral fundamental stiffness converge to the exact equilibrium tangent stiffness; and imposing $\delta = 0$ recovers the published QZS equilibrium condition.

The Taylor expansion in Section 2.2 then reduces to the classical cubic benchmark used for its local frequency-response approximation. These identities verify the nondimensionalization, restoring-force implementation, and viscous/small-amplitude harmonic-balance limit. They do not replace device-level experimental validation, which remains outside the scope of the present computational study.

6.2. Nominal frequency-response comparison

The nominal transmissibility curves and relative displacement amplitudes are shown in **Figure 3**. The linear reference has a large resonance peak and does not enter sustained isolation until $r = 1.418$. All QZS designs move the isolation threshold to a much lower frequency. The viscous-limit design gives the strongest high-frequency mean attenuation, whereas the deterministic fractional design gives the smallest nominal peak. The proposed IT2-robust design lies between them nominally because its objective sacrifices a small amount of nominal sharpness to reduce sensitivity under uncertainty.

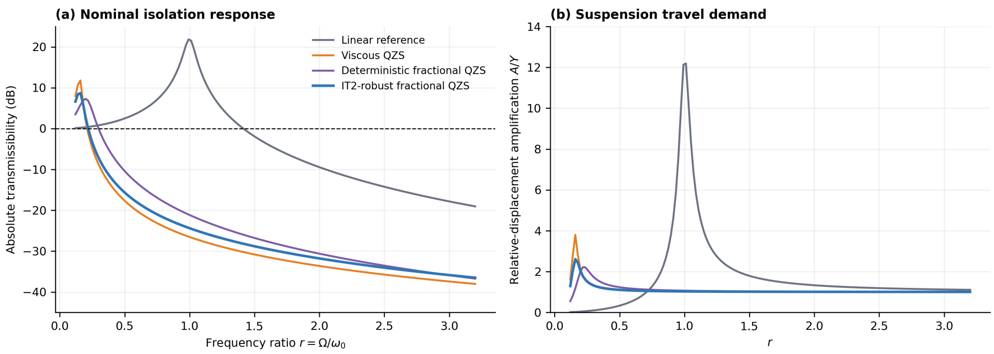

Figure 3. Nominal absolute displacement transmissibility and relative-motion amplitude for the linear, viscous-limit QZS, deterministic fractional QZS, and IT2-robust fractional QZS designs.

Table 4 gives the complete nominal metrics. Relative to the linear support, the proposed design reduces the peak from 12.378 to 2.716, advances the sustained isolation onset from 1.418 to 0.236, and changes the average 1.2–3.0 spectral level from −9.10 to −31.90 dB. The relative-motion ratio will also drop from 12.19 to 2.61. The deterministic fractional design, meanwhile, has a nominal peak of only 2.318 but does not enter sustained isolation until $r = 0.314$.

Table 4. Nominal performance metrics on the 160-point response grid.

Design	Peak T	Isolation onset r_{iso}	Mean level (dB)	95th level (dB)	Max. $A/\bar{Y}$
Linear reference	12.3783	1.4179	−9.0955	3.3744	12.1853
Viscous-limit QZS	3.8861	0.2169	−33.7162	−29.3007	3.7981
Deterministic fractional QZS	2.3178	0.3137	−30.7712	−24.7611	2.2180
IT2-robust fractional QZS	2.7161	0.2362	−31.8970	−27.2310	2.6082

6.3. Root topology and sweep consistency

All of the positive roots in the low-frequency region were solved using a nonlinear amplitude equation. The root cloud with upward and downward continuation is shown in **Figure 4**. Only one accessible root is found at each test frequency for the nominal excitation $\bar{Y} = 0.025$, with both continuation directions overlapping to plotting accuracy. Therefore, the nominal design itself does not exhibit branch-based step discontinuity in the above specified range. This is an important result of the robust input shape rather than an assumption: a nearby QZS design with smaller δ or larger excitation amplitudes can develop multiple roots.

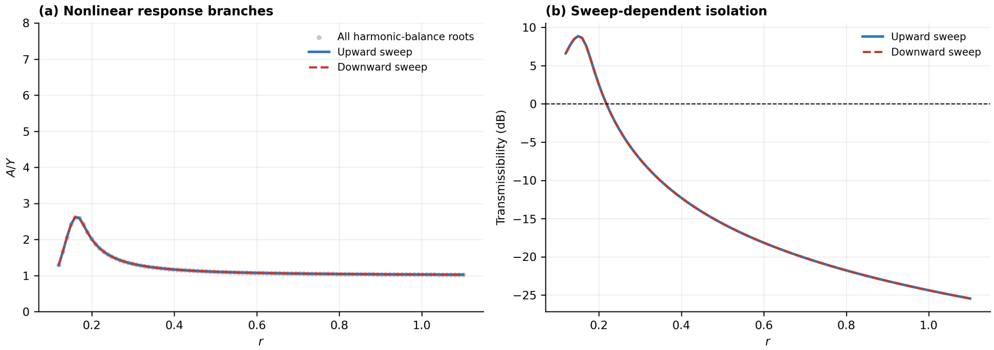

Figure 4. Positive roots of the exact fundamental amplitude equation, and upward/downward frequency continuation at the same level of excitation.

The presence (or absence) of a fold at nominal amplitude is not synonymous with global linearity. The results also show that the resonance location and peak are also amplitude dependent. This indicates that the operating point selected does not cause branch ambiguity under design excitation, and increases a passive device's reliability in slow frequency sweeps. The reliability claim is therefore restricted to the existence and continuation of the reported nominal steady-state branch; it is not a certification of fractional orbital stability.

6.4. Multi-harmonic verification

Figure 5 compares the exact-fundamental response with the five-harmonic AFT result and reports higher-harmonic ratios and residual norm. The curves are visually indistinguishable over most of the frequency range. The largest third-harmonic ratio is approximately 1.112×10^{-3} near the lowest verified frequency, and the fifth-harmonic contribution is below 1.096×10^{-6}. The residual remains at the numerical round-off scale.

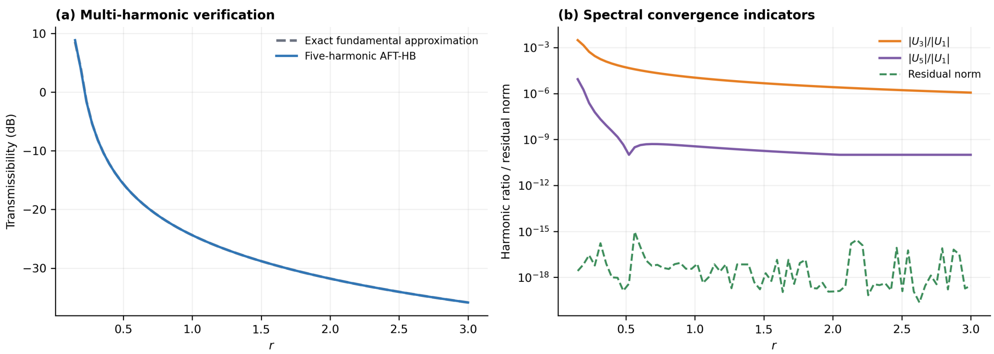

Figure 5. AFT harmonic-balance verification: transmissibility, third- and fifth-harmonic ratios, and nonlinear algebraic residual.

Representative values are listed in **Table 5**. At $r = 0.20$, the one-harmonic transmissibility is 1.341591 and the five-harmonic value is 1.341724, a relative difference below 0.01%. Above $r = 0.28$, the difference is below the displayed sixth decimal place. The five-harmonic residual norms are between 2.02×10^{-19} and 3.47×10^{-18}. These results justify the use of the exact fundamental stiffness during the global design search while retaining the AFT solution as a verification layer.

Table 5. Harmonic-order verification for the proposed design.

r	T_{H1}	T_{H3}	T_{H5}	Residual norm	$\|U_3\| / \|U_1\|$	$\|U_5\| / \|U_1\|$
0.20	1.341591	1.341724	1.341724	2.29×10^{-18}	1.11×10^{-3}	1.10×10^{-6}
0.28	0.509910	0.509914	0.509914	8.94×10^{-19}	2.60×10^{-4}	5.09×10^{-8}
0.40	0.243025	0.243025	0.243025	3.20×10^{-19}	8.92×10^{-5}	3.44×10^{-9}
0.60	0.123605	0.123605	0.123605	3.93×10^{-19}	3.32×10^{-5}	4.23×10^{-10}
1.00	0.060365	0.060365	0.060365	3.47×10^{-18}	1.09×10^{-5}	3.57×10^{-10}
1.60	0.033556	0.033556	0.033556	2.02×10^{-19}	4.12×10^{-6}	1.60×10^{-10}
2.40	0.020818	0.020818	0.020818	4.26×10^{-19}	1.81×10^{-6}	7.36×10^{-11}
3.00	0.016116	0.016116	0.016116	6.55×10^{-19}	1.15×10^{-6}	4.75×10^{-11}

6.5. IT2 fuzzy parameter representation

The upper and lower membership functions for all five uncertain quantities are shown in **Figure 6**. The narrow LMF cores represent parameter values consistently judged plausible, whereas the wider UMF supports represent the full tolerance envelope. The large relative footprint assigned to δ reflects the fact that a small residual stiffness is formed by cancellation of larger positive and negative stiffness contributions. A modest absolute manufacturing error can therefore become a large relative error in δ.

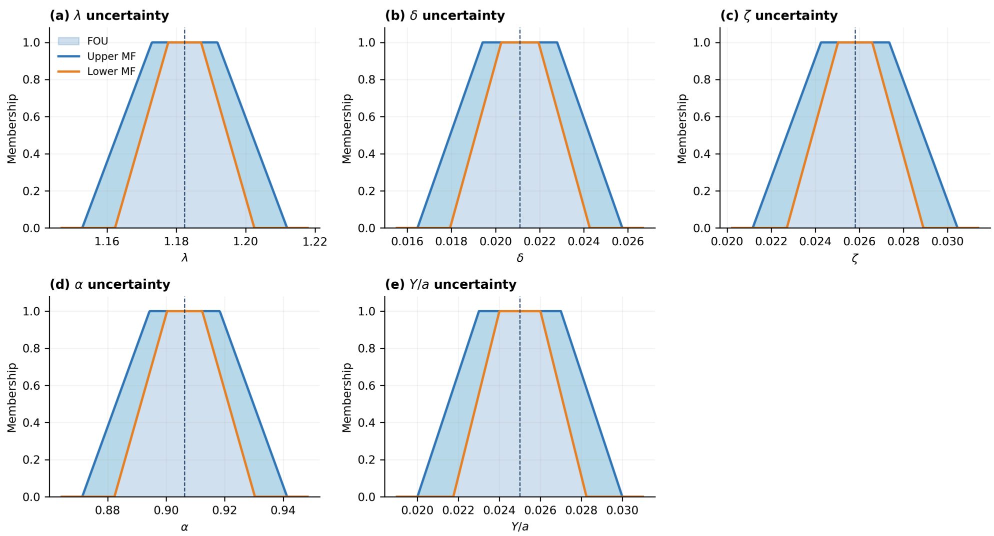

Figure 6. Upper and lower trapezoidal membership functions defining the interval type-2 fuzzy footprints for the five uncertain quantities.

This representation separates two questions that are conflated by a single interval: which parameter values remain physically credible, and which subset has stronger agreement. It also avoids assigning a normal, uniform, or beta density that cannot be supported by data.

6.6. Frequency-wise uncertainty envelopes

The outer-footprint and core-footprint response envelopes for the proposed design are plotted in **Figure 7**. Most of the uncertainty is near the low-frequency resonance; at higher frequencies, the curves collapse into a narrow attenuation band. The core envelope is substantially tighter than the outer envelope, indicating that the broad resonance hazard originates at the uncertain fringe of the IT2 footprint, not in its central membership region.

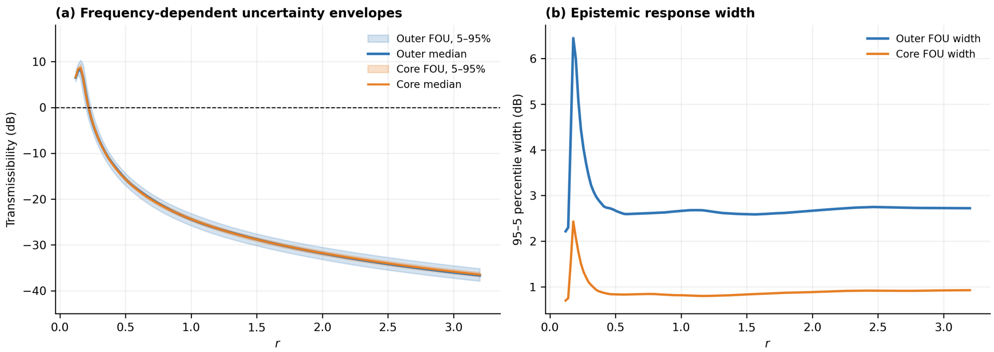

Figure 7. Frequency-wise transmissibility envelopes generated from outer and core regions of the proposed design's IT2 fuzzy footprint.

The envelope is asymmetric because the mapping from parameter intervals to resonance response is nonlinear. In particular, decreasing δ lowers the small-amplitude frequency but can increase the resonance amplification, whereas increasing ζ usually reduces the peak and improves high-frequency attenuation. Opposing parameter effects prevent the response footprint from being estimated reliably by symmetric error bars.

6.7. Alpha-plane contraction

Figure 8 shows the contraction of the peak-transmissibility, isolation-onset, and mean-level summaries as the membership level increases from the outer support ($\eta = 0$) toward the core ($\eta = 1$). The peak interval contracts most visibly. The isolation onset occupies only a few grid values because it is defined by the first sustained threshold crossing, but its upper tail also decreases as the footprint contracts.

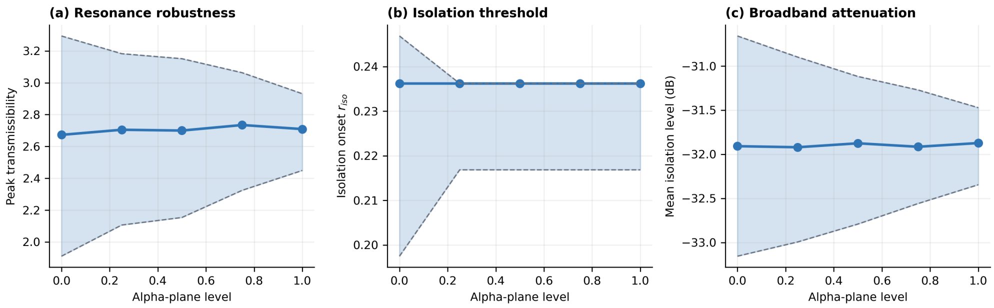

Figure 8. Contraction of performance summaries across nested alpha-planes of the proposed interval type-2 fuzzy design.

The numerical alpha-plane summaries are contained in **Table 6**. At $\eta = 0$, the 5th–95th peak range is 1.910–3.294; at $\eta = 1$, it contracts to 2.449–2.931. The median remains close to 2.70, indicating that the robust optimum is not being driven by a large displacement of the central response. Instead, its principal effect is to constrain the upper resonance tail.

Table 6. Alpha-plane performance summaries for the proposed robust design.

η	Peak T, 5%	Peak T, 50%	Peak T, 95%	r_{iso}, 5%	r_{iso}, 50%	r_{iso}, 95%	Mean dB, 5%	Mean dB, 50%	Mean dB, 95%
0.00	1.910	2.673	3.294	0.197	0.236	0.247	−33.155	−31.909	−30.659
0.25	2.106	2.705	3.183	0.217	0.236	0.236	−32.994	−31.920	−30.898
0.50	2.153	2.700	3.152	0.217	0.236	0.236	−32.791	−31.875	−31.118
0.75	2.324	2.735	3.064	0.217	0.236	0.236	−32.559	−31.915	−31.271
1.00	2.449	2.709	2.931	0.217	0.236	0.236	−32.345	−31.873	−31.472

6.8. Robust comparison across 120 outer-footprint scenarios

Figure 9 compares the distributions of the three optimized QZS designs under the same 120 standardized outer-footprint scenarios. Deterministic fractional tuning has a narrow and low nominal peak but a later isolation onset. The viscous-limit design gives strong broadband attenuation but a long upper tail in the resonance peak. The proposed design compresses that upper peak tail while retaining an early onset and high attenuation.

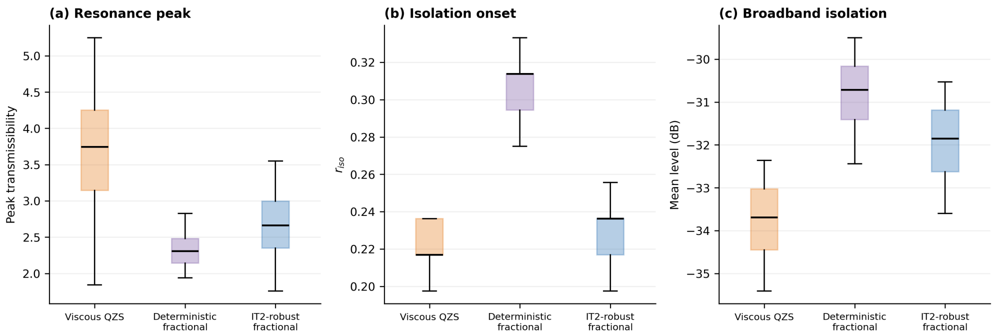

Figure 9. Outer-footprint performance distributions for the viscous-limit, deterministic fractional, and IT2-robust fractional QZS designs.

Table 7 reports the 5th, median, and 95th percentile of every metric. The proposed design's 95th-percentile peak is 3.3579, compared with 4.7232 for the viscous-limit QZS reference, giving a 28.9% reduction. Its 95th-percentile isolation onset is 0.2556, compared with 0.3331 for deterministic fractional tuning, corresponding to a 23.3% earlier onset. Its adverse-tail mean isolation level is −30.735 dB, which is 1.08 dB more attenuating than the deterministic design. The optimum solution trades a later adverse-tail onset (8.2% for the viscous-limit design), and less mean attenuation (1.82 dB) but far smaller risk of resonance. This is the key robust trade-off found by the optimization.

6.9. Pareto structure and parameter sensitivity

This nonconvex trade-off is apparent in the design-space cloud of **Figure 10**. Lower residual stiffness encourages isolation but increases peak sensitivity; higher damping lowers the peak but incurs a material or device requirement penalty. The location of the robust optimum is instead near the knee of the set sampled on nondominated solutions rather than at an extreme minimum of any single nominal metric.

Table 7. Outer-footprint performance quantiles from 120 independent scenarios.

Design and quantile	Peak T	r_{iso}	Mean level (dB)	95th level (dB)	Max. $A/\bar{Y}$
Viscous-limit, 5%	2.2374	0.1975	−35.0425	−30.5155	2.9645
Viscous-limit, 50%	3.7452	0.2169	−33.6903	−29.2398	3.6406
Viscous-limit, 95%	4.7232	0.2362	−32.5584	−28.2079	4.6487
Deterministic fractional, 5%	2.0308	0.2750	−31.9760	−25.9747	1.9456
Deterministic fractional, 50%	2.3050	0.3137	−30.7205	−24.7288	2.2304
Deterministic fractional, 95%	2.7628	0.3331	−29.6593	−23.7202	2.6963
IT2 robust, 5%	1.9525	0.1975	−33.2224	−28.4860	2.1443
IT2 robust, 50%	2.6635	0.2362	−31.8576	−27.1934	2.6293
IT2 robust, 95%	3.3579	0.2556	−30.7354	−26.1121	3.2352

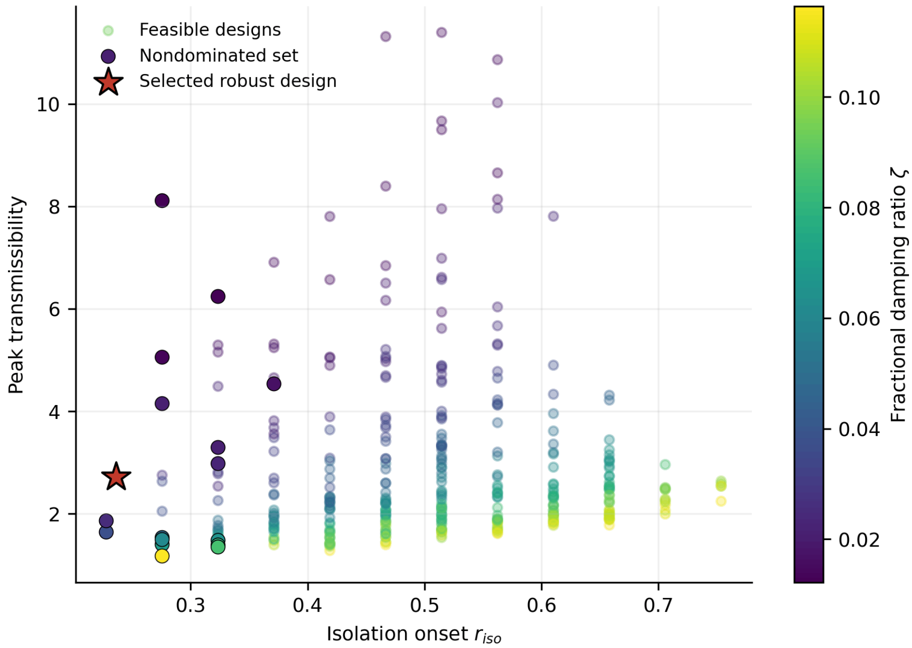

Figure 10. Sampled multi-objective design space, approximate nondominated set, and locations of the three optimized QZS designs.

Spearman sensitivities are plotted in **Figure 11** and reported in **Table 8**. Peak transmissibility and isolation onset are most positively correlated with residual stiffness δ (rank coefficients 0.771 and 0.902, respectively). Fractional damping ζ is negatively correlated with the peak transmissibility (−0.672), and positively associated almost one-to-one with the mean dB metric (0.992)—higher ζ reduces this level after a certain point, as more negative mean dB is better, so this sign indicates that it makes the average level less negative, indicating increased transmission. The order of the derivative α shows less causal relationship with onset but is still an important effect. Secondarily, within the adopted tolerance footprint are geometry λ and amplitude $\bar{Y}$. Spearman coefficients identify monotonic associations only and do not quantify interactions among inputs. Sobol or other variance-based decompositions could provide main- and total-effect indices once defensible probability distributions are available; they were not computed here because the present inputs are possibility footprints rather than probabilistic distributions.

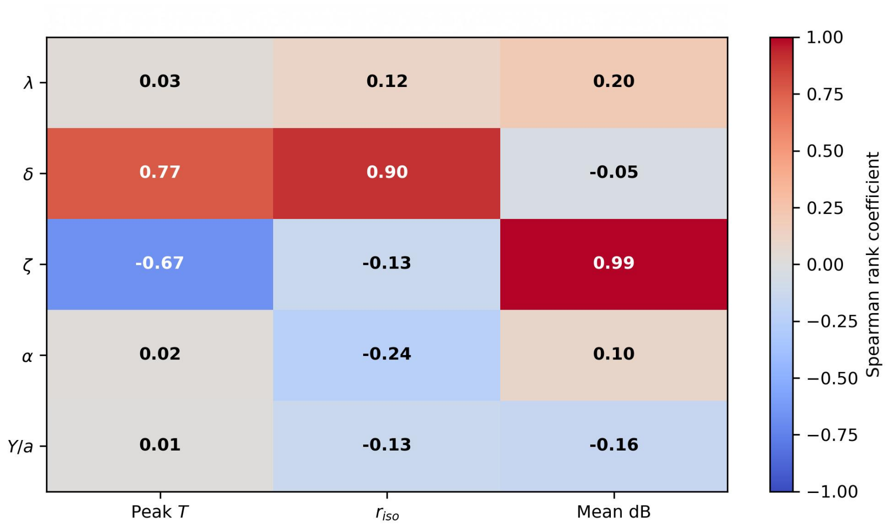

Figure 11. Spearman rank sensitivity of the proposed design's uncertain inputs to resonance peak, isolation onset, and mean isolation level.

Table 8. Spearman rank coefficients for outer-footprint uncertainty propagation.

Uncertain input	Peak T	Isolation onset	Mean level (dB)
λ	0.026	0.117	0.196
δ	0.771	0.902	−0.047
ζ	−0.672	−0.125	0.992
α	0.019	−0.239	0.095
$\bar{Y}$	0.006	−0.126	−0.156

This pattern has a clear engineering interpretation. The manufacturing control should be based on the residual stiffness balance instead of purely the absolute spring stiffnesses. The uncertainty of damping governs broadband attenuation, meaning damping characterization must be performed over the operating frequency range. The relatively weak sensitivity to λ within the adopted $\pm 2.5\%$ range means that geometry is not generally irrelevant; but the robust optimum puts λ in a region where its local effect is weaker than the cancellation error defined by δ.

6.10. Excitation-amplitude dependence

The proposed design was assessed beyond its stated base-motion ratio to characterize the nonlinear performance boundaries. As previously described the response is still well controlled for $\bar{Y} \leq 0.05$ (**Figure 12**), but the resonance peak and isolation onset increase sharply with increasing excitation beyond this level.

The complete metrics are given in **Table 9**. Increasing the base-motion ratio from 0.01 to 0.05 changes the peak from 2.497 to 3.178 and leaves the onset near 0.236. At a base-motion ratio of 0.08, the peak increases to 4.851 and onset to 0.333. The peak of the response at a base-motion ratio of 0.12 is 12.523, and the sustained isolation onset starts at 0.721. Thus, the robust design is not amplitude invariant; rather, its suggested operating envelope must be linked to the range of base-motion that was used for defining the IT2 footprint. This sweep also quantifies the practical boundary of the branch-screened conclusion: relative to the peak of 3.178 at a base-motion ratio of 0.05, the peak rises by 52.6% at 0.08 and by 294.1% at 0.12. Consequently, performance beyond 0.05 should not be inferred from the optimized uncertainty footprint. Engineers should calculate the application's maximum base-motion ratio using the same nondimensionalization, confirm that it does not exceed 0.05, and verify that the identified geometry, residual stiffness, damping intensity, fractional order, and excitation remain inside the outer supports in **Table 2**. Any exceedance requires a new uncertainty footprint, propagation analysis, and re-optimization.

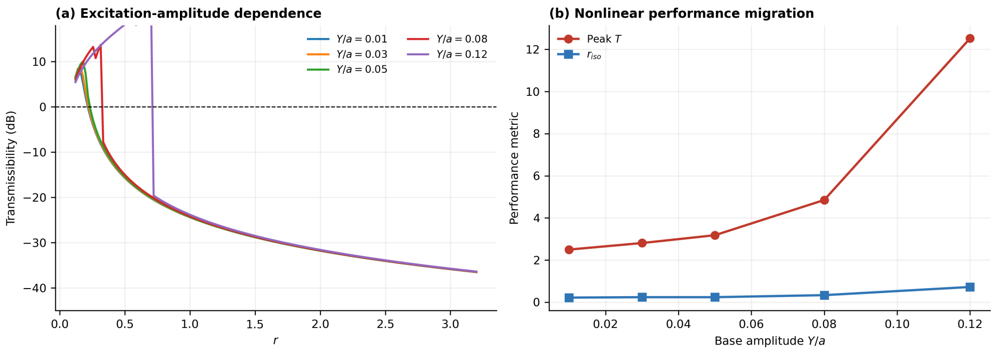

Figure 12. Amplitude-dependent transmissibility of the proposed design and variation of its principal performance metrics.

Table 9. Excitation-amplitude dependence of the proposed design.

$\bar{Y}$	Peak T	r_{iso}	Mean level (dB)	95th level (dB)	Max. $A/\bar{Y}$
0.01	2.4966	0.2169	−31.9049	−27.2449	2.5403
0.03	2.8067	0.2362	−31.8928	−27.2237	2.6169
0.05	3.1781	0.2362	−31.8684	−27.1808	2.9639
0.08	4.8511	0.3331	−31.8077	−27.0741	5.1280
0.12	12.5235	0.7205	−31.6781	−26.8462	12.7637

6.11. Grid and AFT convergence

Table 10 reports the frequency-grid refinement study used to assess numerical convergence. For 160 points or more, the mean isolation level remains stable to within ∼0.02 dB. Since a resonant peak can straddle equally spaced grid points, this causes the sampled peak to oscillate; therefore, we verified that the final location of the peak values lay within a local extremum around the resonant peak. Given its threshold-based definition, it has a lag of one or two grid increments before turning on. The same displayed digits were obtained for AFT time-grid refinements at representative frequencies of 128, 512 and 2,048 phase samples; residual norms were at the round-off scale.

Table 10. Numerical convergence of the proposed design.

Frequency points N_r	Peak T	r_{iso}	Mean level (dB)	95th level (dB)	Max. $A/\bar{Y}$
60	2.2889	0.2244	−31.9274	−27.3215	2.5561
90	2.7672	0.2238	−31.9714	−27.4101	2.5404
120	2.3067	0.2235	−31.9143	−27.2513	2.5633
160	2.7161	0.2362	−31.8970	−27.2310	2.6082
220	2.6404	0.2325	−31.8982	−27.2174	2.6338
320	2.7182	0.2262	−31.9134	−27.2086	2.6101

Peak-response accuracy does not necessarily mean a uniform grid; this is demonstrated through the convergence study. That is, the broadband averages are fairly robust to noise but peak extraction requires an adaptive frequency refinement or local maximisation via continuation. These comparisons are strong because they apply the same grid and branch-tracking rule to each design and scenario, establishing a baseline for comparison across all three.

7. Discussion

Residual stiffness balance explains the difference obtained between the robust solution and deterministic optimum around equilibrium. QZS is primarily optic cancellation near equilibrium Residual parameter δ = positive vertical contribution + negative tangent contribution of the upward-angled springs Optimising solely the nominal curve can drive such cancellation to its limit-case, diminishing peak or on-set of the nominal at the expense of accelerative sensitivity to small perturbations. The IT2 robust objective, on the other hand, takes $\delta = 0.02110$ which is slightly above but not below the prescribed stability margin and a fractional order of 0.9063. Consequently, the specified design should have enough conservativeness (high nominal peak) but not too much (excessive uncertainty upper tail).

There are two aims that the fractional order serves. The imaginary part dictates the loss of energy, while its real part changes dynamic stiffness. When $\alpha < 1$, the memory term stays a fluid-like entity and has finite storage capacity. Although the stiffness-damping balance helps nominal, a deterministic design chooses a much lower order of (0.6146). That balance, however, produces a later isolation onset under uncertainty. This comparison also provides an illustration of why a fractional derivative should not be tuned only as a damping exponent, but rather as part of the complex dynamic stiffness. The analytical elliptic-integral stiffness result is useful. It reduces the first harmonic of the true square-root force to an amplitude-only scalar function, enabling rapid repeated solution with no cubic polynomial replacement. AFT results illustrate the fundamental model is accurate within the selected operating envelope. This is not a guaranteed agreement for all QZS systems. Devices with clearance, friction, impact, asymmetric geometry or very large excitation produce significantly higher harmonics and AFT becomes the required solution method rather than a confirmation layer. Accordingly, for excitation above a base-motion ratio of 0.05 or for a different QZS restoring law, the retained harmonic order and time-grid resolution must be increased until the principal metrics and residual are unchanged within a prescribed tolerance; the present third-harmonic result below 0.31% should not be extrapolated outside the verified range.

IT2 fuzzy modelling is suitable for early-stage design because reliable probability distributions for spring stiffness, geometry, damping, and excitation are often unavailable. In many applications, the available knowledge consists of manufacturing tolerances, supplier ranges or diverging expert judgments. That imprecision is preserved by the UMF–LMF footprint. Alpha-plane results also reveal more than a single worst-case interval: they specify how fast the response range contracts from outer support to core regions. These results should be interpreted as a trade-off, rather than universal superiority. Not every nominal metric is best for the proposed design. The viscous-limit design yields roughly 1.82 dB improved adverse-tail mean attenuation, and the deterministic fractional has a smaller nominal peak. The proposed design is preferable only under the adopted multi-criteria priority. Applications that require maximum high-frequency attenuation, but can tolerate some resonance, will reasonably choose a different point on the Pareto set.

This sensitivity testing identifies practical quality-control priorities. It should be noted that residual stiffness is only determined post-assembly as it accumulates errors in k_v, k_h, l_0, and a; therefore, controlling an individual component cannot simply ensure cancellation. The residual stiffness δ can be directly estimated from a static force–displacement test around equilibrium. The fractional damping parameters should then be identified using either complex stiffness or free-decay data over the relevant frequency range. These two measurements cover most of the sensitivity channels shown in **Figure 11**.

From a more general sound-and-vibration angle, the investigation illustrates how analytical nonlinear mechanics, frequency-domain numerical methods, and soft-computing uncertainty can be combined as opposed to using a black-box predictor to replace physics. The governing equations are defined directly with fuzzy variables, and all response components are the result of the subsequent nonlinear dynamics. Notably, this keeps traceability: at any adverse response, one can trace back the parameter departure from normality, gross aggregate change with dynamic stiffness over all modes and its relation to the transmissibility curve feature.

The relevant QZS research has primarily progressed compliant, magnetic [5–9], metamaterial [10–14] and tested mechanisms, whilst inputs for type-2 fuzzy structural-vibration research have been predominantly active controllers or flesh out fuzzy inference [29, 31, 32]. Thus, the current contribution is not a first new approach to fuzzy nonlinear vibration analysis; it is instead a narrower integration of parameter-level IT2 footprints with precise passive QZS geometry, fractional damping, robust co-design and independent multi-harmonic verification. If we can not harmonise payload, size, damping law and excitation (noise) definitions and uncertainties about each of these, there is as yet no need to discuss direct numerical ranking of magnetic or compliant or metamaterial (QZS-type) passive works. A more universal benchmark for operability should configure each candidate in the same dimensionless parameters to evaluate load capacity, bandwidth, stroke, stability margin and manufacturability at equal uncertainty; hence, the benefits indicated above are constrained to three references.

Comparison of the limiting case with the classical three-spring model [2, 3, 37] confirms both the nondimensional force law and viscous/small-amplitude harmonic-balance limit. Independently, the AFT comparison confirms harmonic truncation within the defined working range. Neither check is equivalent to experimental validation or fractional Floquet certification and thus the conclusions are limited to computational steady-state performance achievable in the relevant amplitude and uncertainty footprints.

8. Limitations and future validation

This research is computational in nature and does not provide experimental validation. The symmetric off-setting springs are modelled as lower-dimensional linear elements; therefore, the influence of joint friction, spring mass, transverse flexibility, non-linear couplings, preload relaxation and contact is ignored. In the Caputo model, one fractional order is assumed to act over the whole frequency range. A distributed-order or multi-term model may be needed if the material is a real viscoelastic material. The values of these fuzzy half-widths are reasonable engineering tolerances that have been selected to stress-test the framework; they should be substituted by measured footprints for a specific prototype. The literature-benchmark limiting cases verify the analytical and numerical implementation, but validation against a fabricated prototype remains necessary before the optimized dimensions are used for hardware design. A distributed-order model would replace the single power-law term with a weighted order spectrum, while a multi-term model would sum several fractional terms; both can represent frequency-dependent storage and loss more flexibly and may shift the optimized resonance-onset trade-off. The present harmonic-balance/AFT framework can accommodate either extension by replacing the single complex fractional factor with the corresponding summed or integrated frequency-domain kernel, while retaining the exact geometric restoring force; the added orders and weights must be identified from material data and the design re-optimized. These adopted uncertainty percentages are not fit to experimental or industrial data; they are author-selected stress-test ranges informed by generic variability in manufacturing, damping, and excitation. Calibrated footprints narrower than model uncertainty would in general contract the response envelopes allowing for a sharper optimum, and broader footprints (or tails) would expand adverse tails of this envelope possibly requiring a shift/against improved stability or increased damping; both cases necessitate some re-optimization and application rather than mere rescaling of reported improvements. Based on a specified payload and inclined-spring stiffness, the dimensional lengths and damping coefficient are mapped from those presented in **Tables 1** and **3**, then the vertical spring is selected to achieve the target assembled residual tangent stiffness. An ideal manufacturing prototype (P) should include adjustable anchor or preload features and be calibrated against static force-displacement and broadband complex-stiffness tests. The primary implementation issues involve keeping symmetric geometry and nearly-cancelling terms under tolerances, realising the fractional element over the target frequency band, controlling friction as well as any joint preloading drift in between, and measuring small low-frequency responses without exciting higher unmodeled modes.

This, however, is a full fractional Floquet stability analysis (unlike the basic pole indicator, which can pick out multiple algebraic roots and proximity to folding but no more). A state-augmentation or frequency-domain Hill method for the fractional variational equation should be developed in future work. Fractional damping parameters based on complex-modulus data should be obtained for future experimental work, and the tangent stiffness of the assembled system should be measured as well as stepped-sine tests at chosen amplitudes. The IT2 footprint is a natural extension of the IT1 footprint where each degree of freedom has associated measurements. Thus, the reported uncertainty quantiles are conditional on that algebraic branch being correct and can be thought of as optimistic if it is later shown to be incorrect. The nominal continuation overlap and the amplitude sweep bound this claim to the stated operating envelope but do not remove the need for fractional Floquet and experimental stability tests.

9. Conclusions

This paper has presented an integrated interval type-2 fuzzy nonlinear vibration-isolation framework for the fractional-order QZS mechanism. The principal findings are:

- This three-spring geometry gives closed-form restoring force, tangent stiffness and potential energy. Unlike cubic truncation directly in the design, its fundamental harmonic can be represented exactly via complete elliptic integrals.
- The storage-like dynamic-stiffness term due to fractional damping combines with a loss term. The optimized robust order $\alpha = 0.9063$ performs significantly differently than the deterministic optimum since uncertainty affects the tradeoff employed between nominal peak reduction and isolation onset.
- Multi-harmonic AFT verification corroborates the fundamental solution in the design envelope. Fifth-harmonic residual norms are on the order of 10^{-18}, and the third-harmonic amplitude ratio is less than 0.31% over the entire verified range.
- For the proposed design, using 120 outer-footprint uncertainty scenarios, the resonance peak at a near-zero QZS condition is attenuated by 28.9% compared to an optimized viscous-limit design reference at the 95th-percentile level. Compared to the deterministic fractional tuning, it advances the adverse-tail isolation onset by 23.3% and enhances the adverse-tail mean attenuation by 1.08 dB.
- Residual tangent stiffness is the dominant uncertainty for resonance and onset, while fractional damping intensity dominates broadband attenuation. Assembly-level stiffness measurement is therefore more important than controlling nominal component values independently.
- The design remains strongly amplitude dependent. Its robust conclusions apply to the stated base-excitation footprint and should not be extrapolated to large excitation without re-optimization.

All equations, uncertainty definitions, numerical settings, optimized parameters, validation samples in summarized form, convergence results, tables, and figures required to inspect the conclusions are contained in this manuscript. The framework can be extended to magnetic, buckled-beam, cam–roller, origami, or multi-degree-of-freedom QZS systems by replacing the restoring-force operator while retaining the fractional AFT and IT2 robust-design layers.

Author contributions: Conceptualization, SIM and YN; methodology, SIM and YN; software, YN and PW; validation, SIM, SAB and PW; formal analysis, SIM and YN; investigation, SIM, YN and SAB; resources, YN, AV and TMAF; data curation, YN and PW; writing—original draft preparation, SIM and YN; writing—review and editing, SIM, YN, SAB, PW, AV and TMAF; visualization, YN and PW; supervision, YN, AV and TMAF; project administration, YN, SIM and AV. All authors have read and agreed to the published version of the manuscript.

Funding: This research received no external funding.

Institutional review board statement: Not applicable.

Informed consent statement: Not applicable.

Data availability statement: All governing equations, parameter values, design bounds, uncertainty definitions, numerical settings, and summarized numerical outputs used to support the findings are contained in the manuscript. No external dataset or supplementary file is required to interpret the reported results.

Conflict of interest: The authors declare no conflict of interest.

AI use statement: During the preparation of this revised manuscript, the authors used ChatGPT (OpenAI) for language refinement verification. No AI tools were used for data analysis, interpretation, or generation of scientific content. All outputs were critically reviewed and edited by the authors. The authors take full responsibility for the integrity and accuracy of the work.

References

1. Ibrahim RA. Recent advances in nonlinear passive vibration isolators. Journal of Sound and Vibration. 2008; 314(3–5): 371–452. doi: 10.1016/j.jsv.2008.01.014
2. Carrella A, Brennan MJ, Waters TP. Static analysis of a passive vibration isolator with quasi-zero-stiffness characteristic. Journal of Sound and Vibration. 2007; 301(3–5): 678–689. doi: 10.1016/j.jsv.2006.10.011
3. Kovacic I, Brennan MJ, Waters TP. A study of a nonlinear vibration isolator with a quasi-zero stiffness characteristic. Journal of Sound and Vibration. 2008; 315(3): 700–711. doi: 10.1016/j.jsv.2007.12.019
4. Carrella A, Brennan MJ, Kovacic I, et al. On the force transmissibility of a vibration isolator with quasi-zero-stiffness. Journal of Sound and Vibration. 2009; 322(4–5): 707–717. doi: 10.1016/j.jsv.2008.11.034
5. Ding B, Li X, Chen SC, et al. Modular quasi-zero-stiffness isolator based on compliant constant-force mechanisms for low-frequency vibration isolation. Journal of Vibration and Control. 2024; 30(13–14): 3006–3020. doi: 10.1177/10775463231188160
6. Sui G, Zhang X, Hou S, et al. Quasi-zero stiffness isolator suitable for low-frequency vibration. Machines. 2023; 11(5): 512. doi: 10.3390/machines11050512
7. Xu D, Yu Q, Zhou J, et al. Theoretical and experimental analyses of a nonlinear magnetic vibration isolator with quasi-zero-stiffness characteristic. Journal of Sound and Vibration. 2013; 332(14): 3377–3389. doi: 10.1016/j.jsv.2013.01.034
8. Zuo S, Wang D, Zhang Y, et al. Design and testing of a parabolic cam-roller quasi-zero-stiffness vibration isolator. International Journal of Mechanical Sciences. 2022; 220: 107146. doi: 10.1016/j.ijmecsci.2022.107146
9. Liu J, Wang Y, Yang S, et al. Customized quasi-zero-stiffness metamaterials for ultra-low-frequency broadband vibration isolation. International Journal of Mechanical Sciences. 2024; 269: 108958. doi: 10.1016/j.ijmecsci.2024.108958
10. Fu J, Huang Z, Li W, et al. A bidirectional-controllable magnetorheological elastomer-based quasi-zero-stiffness isolator. Smart Materials and Structures. 2024; 33(8): 085009. doi: 10.1088/1361-665X/ad53ad
11. Chai Z, Zhang Z, Xu K, et al. An innovative nonlinear bionic X-shaped vibration isolator enhanced by quasi-zero stiffness characteristics: Theory and experimental investigation. Applied Mathematics and Mechanics (English Edition). 2025; 46(8): 1475–1492. doi: 10.1007/s10483-025-3277-8
12. Lu JJ, Yan G, Qi WH, et al. Integrated vibration isolation and actuation via dual nonlinear stiffness regulation. International Journal of Mechanical Sciences. 2024; 263: 108760. doi: 10.1016/j.ijmecsci.2023.108760
13. Yang JH, Yang XD. Theoretical and experimental study of a novel nonlinear quasi-zero-stiffness vibration isolator based on a symmetric link-rod-type structure. Engineering Structures. 2024; 301: 117284. doi: 10.1016/j.engstruct.2023.117284
14. Ma Z, Zhou R, Yang Q. Recent advances in quasi-zero stiffness vibration isolation systems: An overview and future possibilities. Machines. 2022; 10(9): 813. doi: 10.3390/machines10090813

15. Bagley RL, Torvik PJ. A theoretical basis for the application of fractional calculus to viscoelasticity. Journal of Rheology. 1983; 27(3): 201–210. doi: 10.1122/1.549724
16. Rossikhin YA, Shitikova MV. Applications of fractional calculus to dynamic problems of linear and nonlinear hereditary mechanics of solids. Applied Mechanics Reviews. 1997; 50(1): 15–67. doi: 10.1115/1.3101682
17. Caputo M. Linear models of dissipation whose Q is almost frequency independent–II. Geophysical Journal International. 1967; 13(5): 529–539. doi: 10.1111/j.1365-246X.1967.tb02303.x
18. Podlubny I. Fractional Differential Equations. Academic Press; 1999.
19. Sedlmayr M, Rysak A. Damping efficiency of the fractional Duffing system and an assessment of its solution accuracy. Journal of Sound and Vibration. 2024; 593: 118690. doi: 10.1016/j.jsv.2024.118690
20. Xie J, Zhao F, He D, et al. Bifurcation and resonance of a fractional cubic nonlinear system. Chaos, Solitons & Fractals. 2022; 158: 112053. doi: 10.1016/j.chaos.2022.112053
21. Cameron TM, Griffin JH. An alternating frequency/time domain method for calculating the steady-state response of nonlinear dynamic systems. Journal of Applied Mechanics. 1989; 56(1): 149–154. doi: 10.1115/1.3176036
22. Detroux T, Renson L, Masset L, et al. The harmonic balance method for bifurcation analysis of large-scale nonlinear mechanical systems. Computer Methods in Applied Mechanics and Engineering. 2015; 296: 18–38. doi: 10.1016/j.cma.2015.07.017
23. Nayfeh AH, Mook DT. Nonlinear Oscillations. John Wiley & Sons; 1979.
24. Urabe M. Galerkin's procedure for nonlinear periodic systems. Archive for Rational Mechanics and Analysis. 1965; 20: 120–152. doi: 10.1007/BF00284614
25. Zadeh LA. Fuzzy sets. Information and Control. 1965; 8(3): 338–353. doi: 10.1016/S0019-9958(65)90241-X
26. Mendel JM, John RIB. Type-2 fuzzy sets made simple. IEEE Transactions on Fuzzy Systems. 2002; 10(2): 117–127. doi: 10.1109/91.995115
27. Karnik NN, Mendel JM. Centroid of a type-2 fuzzy set. Information Sciences. 2001; 132(1–4): 195–220. doi: 10.1016/S0020-0255(01)00069-X
28. Mohammad AAS, Yogeesh N, Mohammad SIS, et al. An intuitionistic fuzzy graph model: Matrix representations and applications. Cybernetics and Information Technologies. 2025; 25(4): 3–19. doi: 10.2478/cait-2025-0030
29. Liu Y, Yin H, Xia B, et al. Interval type-2 fuzzy set-theoretic control design for uncertain dynamical systems. International Journal of Fuzzy Systems. 2024; 26(3): 1069–1087. doi: 10.1007/s40815-023-01654-3
30. Coupland S, John R. Geometric type-1 and type-2 fuzzy logic systems. IEEE Transactions on Fuzzy Systems. 2007; 15(1): 3–15. doi: 10.1109/TFUZZ.2006.889764
31. Zhang C, Liu M, Mohammadzadeh A, et al. A fractional adaptive type-2 fuzzy structural control system: Theoretical/experimental study. Structures. 2024; 70: 107843. doi: 10.1016/j.istruc.2024.107843
32. Chang YH, Chan WS. Adaptive dynamic surface control for uncertain nonlinear systems with interval type-2 fuzzy neural networks. IEEE Transactions on Cybernetics. 2014; 44(2): 293–304. doi: 10.1109/TCYB.2013.2253548
33. Storn R, Price K. Differential evolution—A simple and efficient heuristic for global optimization over continuous spaces. Journal of Global Optimization. 1997; 11(4): 341–359. doi: 10.1023/A:1008202821328
34. Das S, Suganthan PN. Differential evolution: A survey of the state-of-the-art. IEEE Transactions on Evolutionary Computation. 2011; 15(1): 4–31. doi: 10.1109/TEVC.2010.2059031
35. McKay MD, Beckman RJ, Conover WJ. A comparison of three methods for selecting values of input variables in the analysis of output from a computer code. Technometrics. 1979; 21(2): 239–245. doi: 10.1080/00401706.1979.10489755
36. Saltelli A, Annoni P, Azzini I, et al. Variance based sensitivity analysis of model output. Design and estimator for the total sensitivity index. Computer Physics Communications. 2010; 181(2): 259–270. doi: 10.1016/j.cpc.2009.09.018
37. Spearman C. The proof and measurement of association between two things. The American Journal of Psychology. 1904; 15(1): 72–101. doi: 10.2307/1412159
38. Chitaoui H, Megnounif A, Benadla Z. Optimal placement of vibration control systems in a smart civil engineering structure. Civil Engineering Journal. 2025; 11(8): 3495–3515. doi: 10.28991/CEJ-2025-011-08-022
39. Chu TSC, Sorilla J, Chua AY. UAV-based structural health monitoring using a two-stage CNN model with Lighthouse localization in GNSS-denied environments. HighTech and Innovation Journal. 2025; 6(2): 398–410. doi: 10.28991/HIJ-2025-06-02-03
40. Majima R, Yamasaki Y, Saito T. Shaking-table test on a multi-story continuous vibration-control system employing pulley amplification mechanism. Civil Engineering Journal. 2025; 11(1): 14–32. doi: 10.28991/CEJ-2025-011-01-02